Received: 16 November 2022 | Revised: 3 April 2023 | Accepted: 3 April 2023

DOI: 10.1111/acel.13853

Aging Cell WILEY

RESEARCH ARTICLE

Spatial resolution of cellular senescence dynamics in human colorectal liver metastasis

Ombretta Garbarino[1] | Luca Lambroia[1,2] | Gianluca Basso[1] | Veronica Marrella[1,3] | Barbara Franceschini[4] | Cristiana Soldani[4] | Fabio Pasqualini[1,5] | Desiree Giuliano[1] | Guido Costa[4,5] | Clelia Peano[3,6] | Davide Barbarossa[1] | Destro Annarita[7] | Andreina Salvati[7] | Luigi Terracciano[5,7] | Guido Torzilli[4,5] | Matteo Donadon[4,5] | Francesca Faggioli[1,3]

[1]IRCCS Humanitas Research Hospital, Rozzano, Milan, Italy

[2]Department of Molecular and Translational Medicine, University of Brescia, Brescia, Italy

[3]Institute of Genetics and Biomedical Research, UoS of Milan, National Research Council, Milan, Italy

[4]Department of Hepatobiliary and General Surgery, IRCCS Humanitas Research Hospital, Rozzano, Milan, Italy

[5]Department of Biomedical Science, Humanitas University, Pieve Emanuele (MI), Italy

[6]Fondazione Human Technopole, Milan, Italy

[7]Department of Pathology, IRCCS Humanitas Research Hospital, Rozzano, Milan, Italy

Correspondence
Francesca Faggioli, IRCCS Humanitas Research Hospital, via Manzoni 56, 20089 Rozzano, Milan, Italy c/o Institute of Genetics and Biomedical Research, UoS of Milan, National Research Council, Italy.
Email: francesca.faggioli@humanitasresearch.it; francesca.faggioli@irgb.cnr.it

Funding information
Italian Ministry of Health, Grant/Award Number: GR- 2016-02363222

Abstract

Hepatic metastasis is a clinical challenge for colorectal cancer (CRC). Senescent cancer cells accumulate in CRC favoring tumor dissemination. Whether this mechanism progresses also in metastasis is unexplored. Here, we integrated spatial transcriptomics, 3D-microscopy, and multicellular transcriptomics to study the role of cellular senescence in human colorectal liver metastasis (CRLM). We discovered two distinct senescent metastatic cancer cell (SMCC) subtypes, transcriptionally located at the opposite pole of epithelial (e) to mesenchymal (m) transition. SMCCs differ in chemotherapy susceptibility, biological program, and prognostic roles. Mechanistically, epithelial (e)SMCC initiation relies on nucleolar stress, whereby c-myc dependent oncogene hyperactivation induces ribosomal RPL11 accumulation and DNA damage response. In a 2D pre-clinical model, we demonstrated that RPL11 co-localized with HDM2, a p53-specific ubiquitin ligase, leading to senescence activation in (e)SMCCs. On the contrary, mesenchymal (m)SMCCs undergo TGFβ paracrine activation of NOX4-p15 effectors. SMCCs display opposing effects also in the immune regulation of neighboring cells, establishing an immunosuppressive environment or leading to an active immune workflow. Both SMCC signatures are predictive biomarkers whose unbalanced ratio determined the clinical outcome in CRLM and CRC patients. Altogether, we provide a comprehensive new understanding of the role of SMCCs in CRLM and highlight their potential as new therapeutic targets to limit CRLM progression.

Abbreviations: CRC, colorectal cancer; CRLM, colorectal liver metastasis; CSs, capture spots; DFS, disease free survival; ECM, extracellular matrix; EMT, epithelial to mesenchymal transition; (e)SMCC, epithelial SMCC; H&E, hematoxylin and eosin; HR, hazard ratio; iSMCC, intermediate SMCC; (m)SMCC, mesenchymal SMCC; OS, overall survival; SA-β-gal, senescence associated β -galactosidase; SMCC, senescent metastatic cancer cell; ST, spatial transcriptomics.

Ombretta Garbarino and Luca Lambroia share the first authorship.

KEYWORDS
cellular senescence, colorectal cancer liver metastasis, EMT, prognostic role, senescence-associated secretory phenotype, spatial transcriptomics

1 | INTRODUCTION

Metastasis is an inefficient process because of the multitude of obstacles that circulating cancer cells meet before successful seeding (Celià-Terrassa & Kang, 2018). Indeed, in a mouse model of melanoma, <0.1% of tumor cells were capable of metastasizing (Luzzi et al., 1998). However, 90% of cancer lethality is due to metastasis (Steeg, 2006). Colorectal liver metastasis (CRLM) is not an exception. CRLM develops in 50% of colorectal cancer (CRC) patients. Surgical resection after neo-adjuvant chemotherapy is the gold standard, but only 10%–20% of patients are eligible (Zhou et al., 2022). CRLM seeding was reported to occur in 80% of CRC cases before the primary tumor was clinically detectable (Hu et al., 2019), indicating that metastasis initiation is an unexpectedly early event.

Cellular senescence is viewed as a desirable outcome for cancer therapy because it represents a state of permanent cell-cycle arrest (Hayflick & Moorhead, 1961; Sieben et al., 2018). Indeed, in this terminal state, cancer cells are still alive but are either not harmful or in an intermediate stage of vulnerability and targetable by senolytic drugs (Naylor et al., 2013; Ovadya & Krizhanovsky, 2018). Senescent cancer cells might also promote immune recruitment for their suicide or signal for the clearance of non-senescent cancer cells through their secretome (Kang et al., 2011; Xue et al., 2007). However, there is evidence also of a cancer-promoting function, including local invasion and epithelial-to-mesenchymal transition (EMT), fueling efforts in targeting senescent cells therapeutically (Ou et al., 2021). To date, translation of pro-senescence compounds to the clinic has focused on primary tumors (Ovadya & Krizhanovsky, 2018) with less attention given to the role of cellular senescence in metastasis. Additionally, studies on chemotherapy-naive metastatic patients are rare, except Haugstetter et al. (2010), who described senescence as a common feature in CRLM and having a positive prognostic role in patient survival. By contrast, senescent cancer cells were found to support tumor spread in colorectal and thyroid cancers (Choi et al., 2021; Kim et al., 2017). These conflicting findings highlight the complex role of cellular senescence in the evolution of cancer from primary to secondary organs (Faggioli et al., 2023).

Here, to study the pathophysiological role of cellular senescence in CRLM, we combined spatial transcriptomics (ST) with the senescence-associated β-galactosidase (SA-β-gal) assay and 3D-microscopy. We define the mechanisms of senescence activation and the role played by chemotherapy. Moreover, integration of data into a multicellular transcriptional database identified the senescent-dependent cancer ecosystems that coexist within CRC and CRLM and that determine the clinical outcome.

2 | RESULTS

2.1 | Tumor cells consistently turn senescent in CRLM

First, we analyzed a small cohort of CRLM patients (Table S1) with the SA-β-gal assay, the gold standard for the detection of pan-senescence (Debacq-Chainiaux et al., 2009; Gorgoulis et al., 2019). 75% of specimens were SA-β-gal-positive in intrametastatic areas (Figure S1a,b). Cell-cycle arrest was confirmed by immunohistochemistry for the CDK2 inhibitor $p21^{Cip1}$ and the CDK4/6 inhibitor $p16^{Ink4a}$, the molecular effectors of the p53- and pRB-sustained senescence pathways (Gorgoulis et al., 2019). As for primary CRC (Choi et al., 2021), SA-β-gal-positive cells accumulated prevalently at the metastatic marginal zone (Figure S1a). The average SA-β-gal-positive area within cancer spanned from 10% to 30% (Figure S1c). No significant correlation was found between clinical parameters and senescence grading (data not shown). However, we confirmed in an independent cohort that cellular senescence is not a stochastic event in CRLM.

2.2 | Deciphering the transcriptional heterogeneity of senescent metastatic cancer cells by generating a whole-transcriptome spatial atlas of human CRLM

We then asked whether it would be possible to dissect the role of cellular senescence within CRC metastasis. We reasoned that any transcriptional approach would not, per se, accurately identify senescent metastatic cancer cells (SMCCs), which lack exclusive markers (Gorgoulis et al., 2019), and that intra-tumor heterogeneity would make deciphering the senescence signature even more difficult. To overcome these limits, we performed ST and SA-β-gal assay on serial cryosections (Figure 1a,b). This approach allowed us to localize β-gal-positive cells within metastases and then to identify overlapping transcriptional clusters through ST on the consecutive section. The data were collected from four post-chemotherapy patients; for each, one hepatic lesion was selected and processed through the Visium Spatial Gene Expression protocol (Figure 1b–d); two metastases were pre-screened with SA-β-gal (Figure 1a and Figure S1d–f). To distinguish senescent cells from not senescent, we first compared the histology of the lesion that underwent ST and the consecutive section stained for β-gal. An expert pathologist, blinded to transcriptional data, identified on ST histological section the areas corresponding to β-gal-positive cells (Figure 1a,b). Then, we identified the transcriptional clusters enriched in β-gal – senescent-like areas

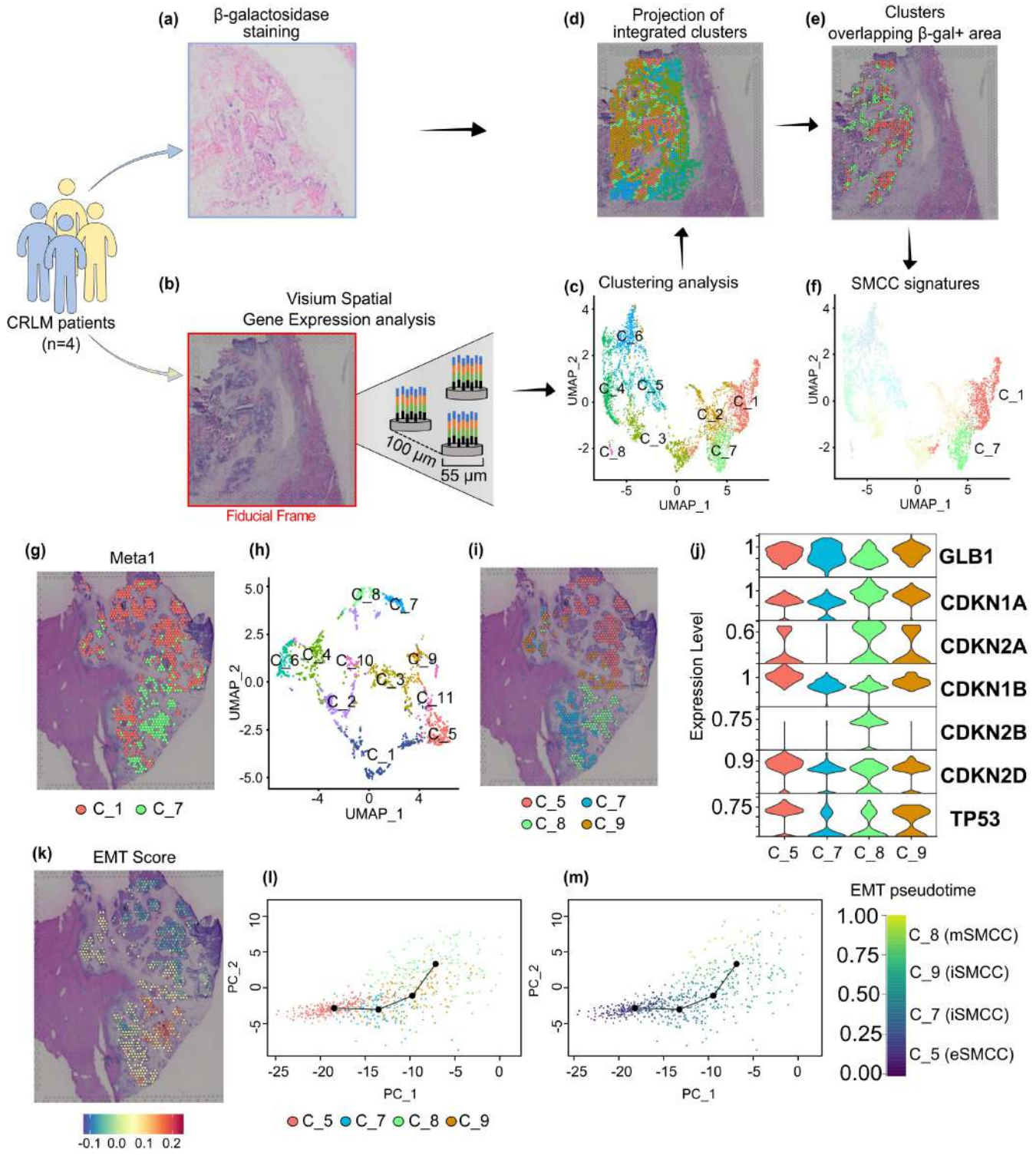

FIGURE 1 Spatial and transcriptional identification of senescent metastatic cancer cells in colorectal liver metastasis (CRLM). (a–f) Workflow of spatial transcriptomics combined with SA-β-gal assay on CRLM specimens. Four liver metastatic biopsies were analyzed with ST technology: Two of them (blue) underwent SA-β-gal assay. (a) A SA-β-gal-positive specimen. (b) Hematoxylin and eosin (H&E) image of a CRLM specimen prior to permeabilization for ST processing. (c) UMAP of ST-integrated analysis. (d) Projection of 8 integrated cancer clusters onto the H&E image acquired before permeabilization. (e) SA-β-gal-positive transcriptional signature projected onto an H&E image. (f) UMAP of two identified senescent cancer clusters: C_1 (salmon) and C_7 (green). (g) Spatial projection of tumoral senescent clusters on meta1. (h) UMAP of individual analysis, showing 11 clusters. (i) Spatial projection of senescent clusters onto the corresponding H&E image. (j) Violin plots of senescence-associated genes in tumoral clusters for the metal specimen. (k) Epithelial-to-mesenchymal transition (EMT) score generated on the EMTome platform. (l) Trajectory generated by PCA on metal genes. (m) Pseudotime trajectory on EMT genes.

(Figure 1e). ST reliably quantified the spatial distribution of >800 genes in individual capture spots (CSs), adding up to 8431 genes/CS over the four biopsies. We detected 4296.25 ± 1106 unique molecular identifiers and 1489 ± 226 unique genes per CS. Integrated gene-expression clustering of the intrametastatic datasets identified eight distinct clusters in 17,874 genes stratified in tumoral crypt and extracellular matrix (ECM) subgroups (Figure 1c). Spatial data were verified to strongly recapitulate CRLM histology (Figure S2a–c). Parenchymal data were not included in further analysis.

Within the transcriptional space, we uncovered two consistently expressed transcriptional programs (C_1 and C_7), later referred to as "senescent metastatic cancer cells" (SMCCs) (Figure 1f). Notably, only in one sample (referred to as meta1) C_1 and C_7 clusters were uniformly located in geographically distinct regions (Figure 1g); in the other three, the clusters were distributed unevenly, like mixed puzzle pieces, making it difficult to address how the cells behaved (Figure S2d).

We, therefore, performed unsupervised individual analysis on the meta1 specimen to get a more accurate gene-expression profile of 16,811 genes, clustered in 11 subgroups (Figure 1h), identifying four distinct transcriptional signatures in the tumoral crypts (C_5, C_7–C_9) overlapping with SMCCs clusters (Figure 1i). All four clusters expressed high levels of galactosidase (GLB1) mRNA (Figure 1j), confirming that even if meta1 was not pre-screened for β-gal activity, active GLB1 transcription proved that the SMCCs were bona fide (Hernandez-Segura et al., 2017). In line with the literature (Kumari & Jat, 2021; Sonzogni et al., 2014), there was an accumulation of $p21^{Cip1}$ and $p16^{Ink4b}$ cyclin inhibitor kinases and $p19^{Ink2d}$, which is involved in senescence related-chromatin compaction, suggesting that redundant mechanisms coexist to reinforce proliferation arrest (Figure 1j). Notably, the cyclin kinase inhibitors $p27^{Kip1}$ (Lloyd et al., 1999) and $p15^{Ink4b}$ (Hannon & Beach, 1994) were differentially expressed in C_5 and C_8, raising the question of whether the properties of these SMCCs subtypes were fundamentally different.

2.3 | SMCCs have EMT-dependent transcriptional programs and different secretomes

Epithelial-to-mesenchymal transition is a reversible process implicated in invasion, tumor stemness, and metastatic spread (Kalluri & Weinberg, 2009). To investigate whether SMCC signatures differed in EMT states, we integrated our spatial data into the EMTome database, which includes an EMT signature of 1153 genes across 32 cancer types (Vasaikar et al., 2021). We assigned an EMT score to each of our CSs based on the expression values of the EMT gene signature (Figure 1k). EMT score mapping revealed that C_8 was enriched in mesenchymal markers, while C_5 was closely related to the epithelial signature. This was confirmed by principal component analysis (PCA) derived trajectories of EMT genes, with C_5 located at the zero EMT state and C_8 at the trajectory extreme, representing a mature mesenchymal phenotype (Figure 1l,m). As a result, we defined C_5 and C_8 as epithelial (e) and mesenchymal (m) SMCCs, respectively. The regulon-enriched analysis also supported these findings (Table S2). C_7 and C_9 signatures were found to be in between the EMT poles and were thus classified as intermediate stages (iSMCCs, Figure 1m, EMT pseudotime).

Expression analysis of ST data of eSMCCs versus mSMCCs identified 349 differentially upregulated genes (Figure 2a and Table S3). Gene ontology analysis of eSMCC-related genes identified enrichment of pathways involved in nucleolar stress (Figure 2b and Table S4) (Boulon et al., 2010; Yang et al., 2018). In contrast, the 229 differentially upregulated genes identified in mSMCCs were enriched for tumor carcinogenesis and micro-environment remodeling (Figure 2c and Table S5), suggesting that mSMCCs undergo functional and structural reprogramming typical of aggressive cancer cells.

Many factors can influence the senescence program. Here, we investigated the SMCCs phenotype related to stress signals and the type of cells, exploiting the Senescence-Associated Secretory Phenotype (SASP) atlas. This comprehensive proteomic database includes the profile of senescent pulmonary fibroblasts and epithelial cells developed from several stressors (Basisty et al., 2020). 24% of eSMCCs genes overlapped with those in the SASP database, while up to 51% of mSMCCs genes were included (Figure 2d,e). These findings indicate SMCCs diverged in terms of the type and magnitude of secretory molecules. Of note, the eSMCC SASP profile recapitulated the signature of RAS oncogene-induced senescent fibroblasts, while fewer similarities emerged in comparison with epithelial irradiated senescent cells (Figure 2d). Additionally, mSMCCs had a more mixed phenotype similar to several inducers, including pharmacological treatment (Figure 2e), suggesting that for SMCCs SASPs complexity was determined by the senescence-stressor inducer.

Mechanistically, SASPs were supported by ubiquitous and SMCC-type related signaling driving upregulation of NFKB1, the master regulator of primarily SASP factors, in both SMCC subtypes (Figure S3a,b) (Salminen et al., 2012).

2.4 | Mechanisms of SMCCs induction

2.4.1 | Nucleolar stress drives the eSMCC signature

Nucleolar stress indicates an impairment of morphological and functional nuclear homeostasis, which lead to the activation of p53 effector (though inhibition of E3 ubiquitin-protein ligase HDM2) and, more often, cellular senescence. Ribosome biogenesis and its transcriptional controller, *c-MYC* (Destefanis et al., 2020), are key regulators of nucleolar integrity and are extensively exploited by eSMCCs as *HDM2* and p53 (Figure 3a–d). To validate involvement in anticancer response, we focused on the highly expressed ribosomal protein RPL11 (Figure 3d), which inhibits p53–HDM2 interaction (Havel et al., 2015; Lohrum et al., 2000). First, through 3-multilabel immunofluorescence on whole sections of meta1, we confirmed that RPL11 accumulated significantly in eSMCCs (Figure 3e). Confocal analysis revealed that when located in the cytoplasm, RPL11 probably takes

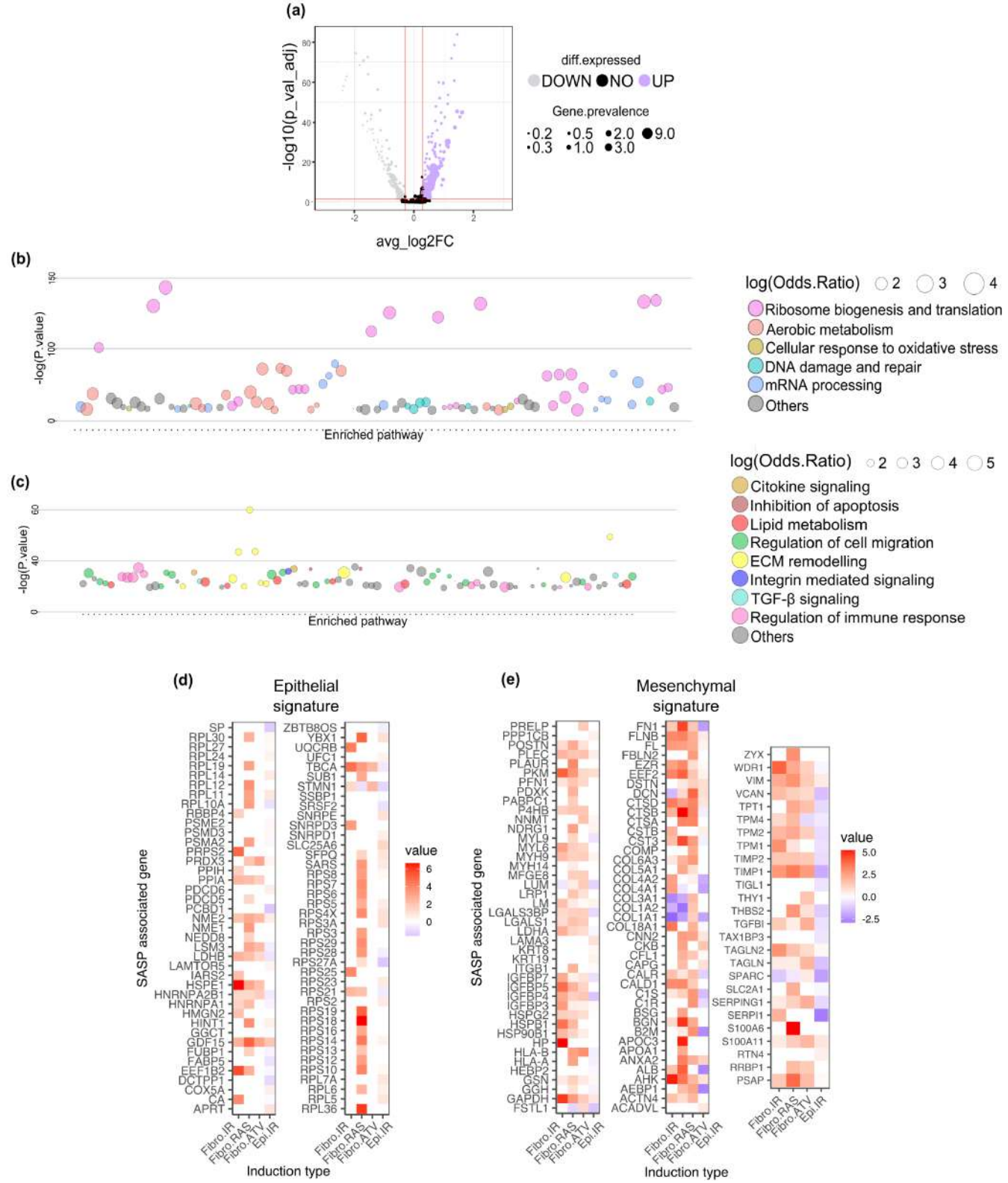

FIGURE 2 eSMCCs and mSMCCs have independent transcriptional programs. (a) Volcano plot of differential expression analysis of eSMCC vs. mSMCCs. Average log2 FC >0.3; adjusted $p < 0.05$. Gene ontology analysis and most-significant pathways are given for eSMCC (b) and mSMCC (c) clusters. Heatmaps of SASP-associated genes for eSMCC (d) and mSMCC (e) signatures, compared with the SASP atlas database.

part in global translation typical of excessive ribosome biogenesis, but when in the nucleoplasm (77% over 181 inspected cells), it interacts with HDM2 (Russo & Russo, 2017). HDM2's activity map overlapped with cells having nucleoplasm-located RPL11 suggesting possible interaction (Figure 3b,e). To validate this hypothesis, we induced cellular senescence in the HCT-116 cell line, in which

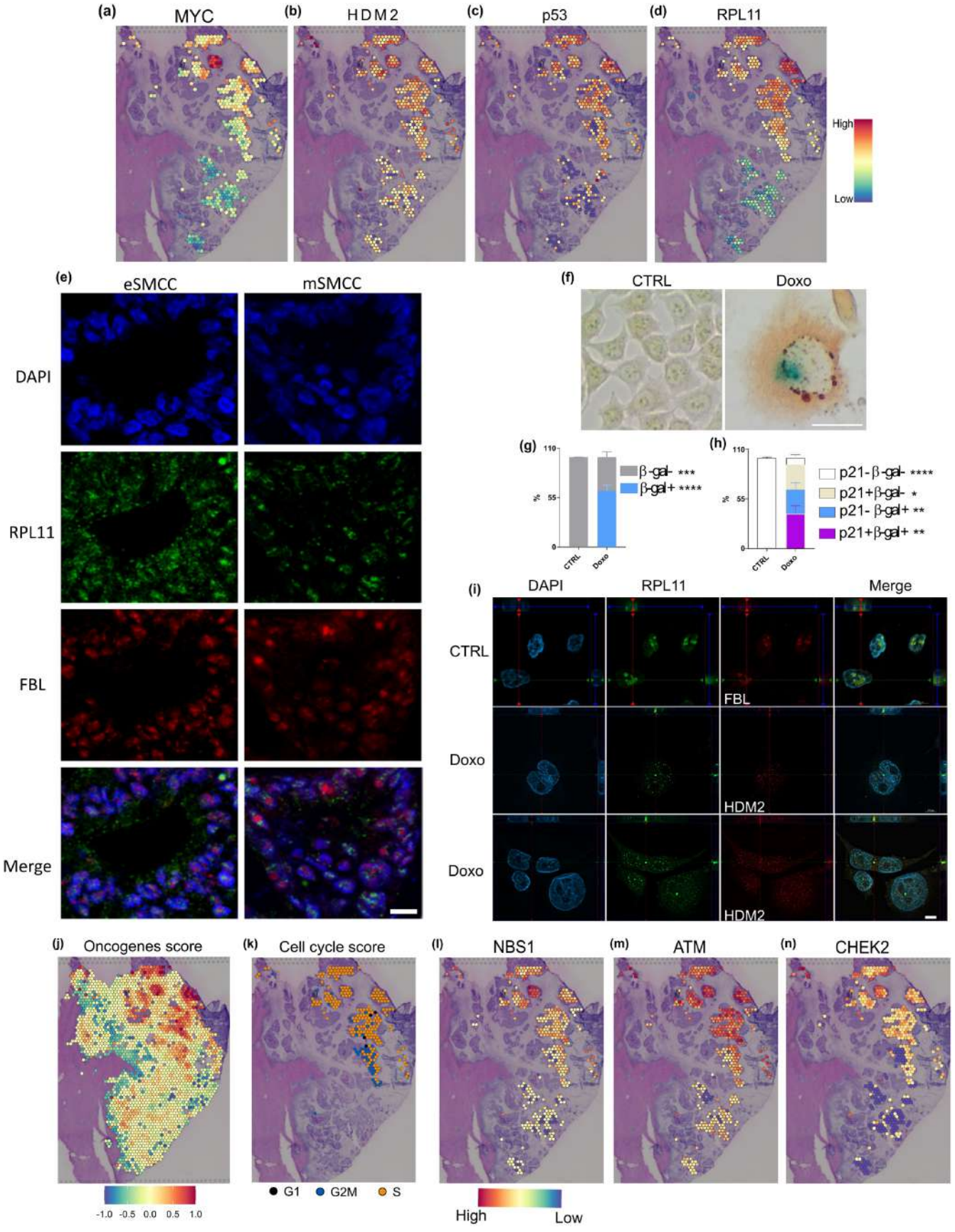

FIGURE 3 Nucleolar stress drives the eSMCC signature. (a–d) Activity maps of genes involved in HDM2-p53 axis. (e) Z-stack projection of RPL11 and FBL immunofluorescence on selected areas of eSMMCs and mSMMCs on meta1, bar 10 μm. (f) Co-staining of p21 protein (brown) and β-gal enzymatic activity (blue) on HCT-116 cell line (CTRL vs. Doxo), bar 100 μm. Quantification of β-gal (g) and p21-positive cells (h) scored by optical evaluation over three experiments. *T* test, $^{*}p < 0.05$; $^{**}p < 0.01$; $^{***}p < 0.001$; $^{****}p < 0.0001$. (i) Representative single focal plane of Z-stacks for RPL11, FBL, and HDM2 immunofluorescence on doxorubicin-exposed HCT-116 cells and control, bar 20 μm. (j) Oncogene activation score. (k) Cell cycle phase analysis. (l) DNA damage sensor, upstream (m) and downstream (n) kinase activity maps.

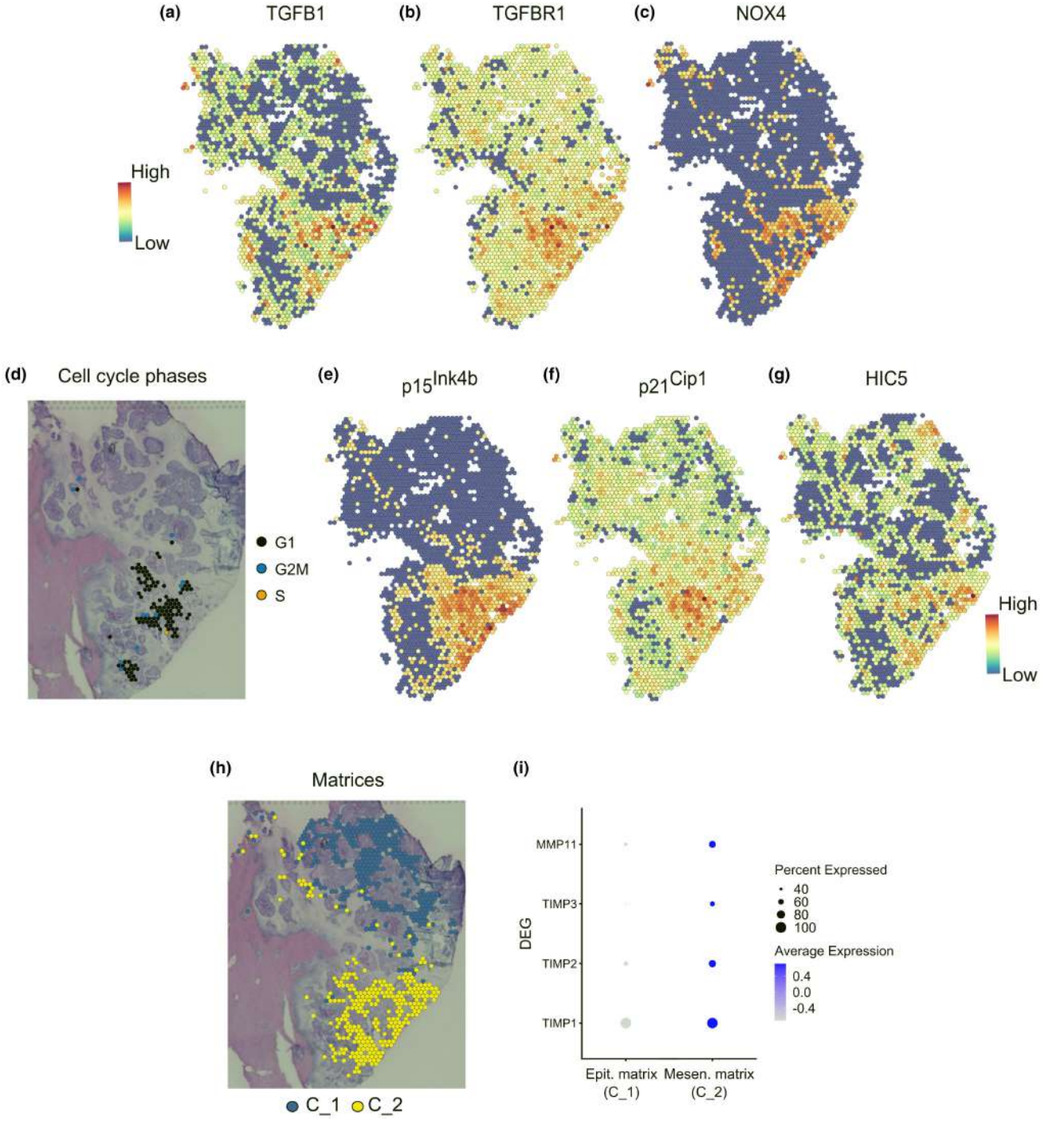

FIGURE 4 Paracrine activation of the mSMCC signature. (a) Activity maps for TGFβ and (b) its cognate receptor, TGFB1. (c) ST distribution of NOX4. (d) Cell-cycle assignment of mSMCCs. Activity maps for $p15^{Ink4b}$ (e), $p21^{Cip1}$ (f) and HIC5 (g) are shown. (h) Extracellular matrix cell cluster localization over meta1 (C1, C2). (i) Differential remodeling factors in extracellular matrix surrounding crypts.

both $p16^{Ink4a}$ alleles are inactivated (Burri et al., 2001) and HDM2-p53-$p21^{Cip1}$-dependent senescence most likely occurs. Doxorubicin (Doxo) is a known chemotherapic agent but also a potent genotoxic ribosomal stress inducer (Morgado-Palacin et al., 2014; Petrova et al., 2016; Was et al., 2018). After its exposure, upregulation of $p21^{Cip1}$ at the protein level confirmed the activation of a p53-dependent senescence phenotype in HCT-116 treated cells, reaching a mean of 62% β-gal-positive cells (Figure 3f–h). Interestingly, not all β-gal-positive cells expressed the p21 protein, most likely due to a delay in the senescence activation program. Interestingly, the transcriptional signature of Doxo-treated HCT-116 cells overlapped with both eSMCC and mSMCC groups, supporting our previous observation that the type of stressor rather than the cell type is a determinant in SMCCs phenotype (Figure S3c–f). Indeed, Doxo as a chemotherapic agent and nucleolar stress inducer is able to activate both phenotypes in the same cell line. Immunofluorescence for RPL11 and HDM2 revealed that RPL11 co-localized with fibrillarin in the basal condition, but that the nucleolar marker was not more present in treated cells, indicative of nucleolar stress (Figure 3i and data not shown). Given the nucleolar disruption, it was not possible to assess the translocation of RPL11 into the nucleoplasm; however, RPL11 and HDM2 were tightly co-localized within the nucleus in >72% of inspected cells; in contrast, 50% of cytoplasmic RPL11 co-localized with HDM2 (Figure 3i), supporting the role of RPL11 as a shuttle for HDM2-mediated proteasomal degradation (Bursać et al., 2012). Therefore, we speculated that excessive free RPL11 in eSMCCs increased the chance of interaction with HDM2 at the nuclear and cytoplasmic levels, driving stabilization of p53 and activation of senescence.

We then reasoned that c-Myc was a proto-oncogene that was not only involved in ribosome biogenesis; indeed, activated oncogenes are prominent inducers of senescence (Braig & Schmitt, 2006). Therefore, we pulled together the expression data of significantly upregulated oncogenes in eSMCCs and generated an oncogene activation score for the epithelial signature, indicative of high mitogenic activity (Figure 3j). As expected, we found genes (e.g., *Braf*, *Fos*) involved in conflicting roles as a tumor promoters or suppressor in various cancers (Mahner et al., 2008; Michaloglou et al., 2008). Excessive mitogenic stimulation was confirmed by the *CellCycleScoring* function (Seurat) of R package, indicative of eSMCCs being synchronized in the S phase (Figure 3k) (Tirosh et al., 2016). This condition was not exclusive to proliferating cells, since oncogene-induced senescent cancer cells can be S-phase arrested (Campisi & D'Adda Di Fagagna, 2007).

The limit on oncogene-induced cell growth is aberrant DNA replication, which in turn generates DNA damage (Campisi & D'Adda Di Fagagna, 2007). Indeed, ST analysis on eSMCCs identified upregulation of molecular factors involved in each step of the DNA damage repair pathway: sensors of single- and double-strand breaks (e.g., NBS1), central regulators of the DNA damage response network (e.g., ATM; Maréchal & Zou, 2013) and downstream kinases (e.g., CHEK2; Figure 3l–n and data not shown). The functional activation of DNA damage repair pathway was confirmed by the co-localization of the phosphorylated form of H2AX and ATR in eSMCC crypts detected by immunofluorescence (Figure S3g; Podhorecka et al., 2010). Thus, oncogene overexpression in eSMCCs overlaps with DNA damage response activation, and most likely contributes to the establishment of senescence.

2.4.2 | TGFβ-dependent paracrine activation of mSMCC cell cycle arrest

Pleiotropic TGFβ can exert cell-autonomous tumor suppressor or pro-tumorigenic effects in cancer (Baba et al., 2022; Massagué, 2008). To understand the multiple consequences of TGFβ activity within mSMCCs, we first confirmed local activation. In meta1, TGFβ1 mainly localized to stroma adjacent to mesenchymal crypts, a finding suggesting that this cytokine is produced, or at least retained, in a latent state by ECM cells (Figure 4a). The TGFBr1 receptor was selectively overexpressed in mSMCCs and corresponding ECM cells (Figure 4b), which were most likely the main targets of TGFβ (vander Ark et al., 2018). Then, to define the impact of TGFβ on SMCCs, we focused on its known anti-proliferative properties. Indeed, TGFβ inhibits proliferation by inducing G1- phase cell-cycle arrest through the activation of NADPH oxidase 4 (*NOX4*) and accumulation of reactive oxygen species, which drive c-MYC down-regulation. In turn, c-MYC negatively regulates $p15^{Ink4b}$ and $p21^{Cip1}$ expression (Baba et al., 2022; Bird et al., 2018; Senturk et al., 2010; Seoane & Gomis, 2017). In line with the literature, we found positive transcriptional activity for *NOX4* in mSMCCs (Figure 4c), down-regulation of *c-MYC* (Figure 3a), G1 phase synchronized cancer cells (Figure 4d), and upregulation of the CDK inhibitory genes $p15^{Ink4b}$ and $p21^{Cip1}$ (Figure 4e,f); the upregulation of hydrogen peroxide-inducible clone 5 (*HIC5*) (Figure 4g), a sensor of free radicals and an antagonist of *NOX4* (Desai et al., 2014; Wolfgang Doppler, 2019), confirmed the tissue response to *NOX4* activation. Notably, *NOX4* as a downstream effector of TGFβ1 might coordinate additional functions in mSMCCs not related to cell-cycle arrest, like EMT, tissue remodeling, and angiogenesis (Chen et al., 2017). To this end, we investigated differences in ECM remodeling factors. As expected, epithelial (C1) and mesenchymal (C2) matrices had opposite profiles (Figure 4h,i): mesenchymal ECM was characterized by higher expression of metalloproteinases (*MMP9*, *MMP2*, *MMP11*) and the corresponding inhibitors (*TIMP1*, *TIMP2*, *TIMP3*). These differences reflected distinct abilities to manipulate the micro-environment and were indicative of effective ECM remodeling in proximity of mesenchymal crypts. All of these features are known to be involved in metastatic spread and poor prognosis (Winkler et al., 2020).

2.5 | Clinical predictions based on the assessment of epithelial and mesenchymal SMCCs in a CRLM validation cohort and an extended CRC database

To investigate the clinical impacts of the eSMCC and mSMMC signatures, we first performed a retrospective analysis (follow-up, ≥10 years) on CRLM samples randomized into chemotherapy-naïve

($n=34$) and treated ($n=34$) groups (Table S1). To identify patients expressing an SMCC-type signature, we established a 5-multilabel serial approach using selected markers of proliferation (ki67), DNA damage (γH2AX), and cell-cycle arrest ($p21^{Cip1}$, $p16^{Ink4a}$, $p15^{Ink4b}$) that had emerged from our previous spatial analysis (Figures 1j and 5a). We classified the 68 patients into four categories following these criteria: eSMCCs were defined by co-expression of $p16^{Ink4a}$, $p21^{Cip1}$, and γH2AX (7.4%); when also $p15^{Ink4b}$ was co-detected, we classified the samples as "Mix" (16.2%); mSMCCs were defined by the co-expression of $p15^{Ink4b}$ with $p16^{Ink4a}$ and or with $p21^{Cip1}$ (38.2%); all the other possibilities were classified as negative (38.2%). The overall quantification of SMCCs and cell cycle inhibitors markers are indicated in Figure 5b,c. With this approach, we spatially dissected the localization of SMCC populations across the metastasis, identifying within the Mix group three cases (4.4%) in which SMCCs were located in two distinct regions (Figure S4a). Contrarily to meta1, we found Mix type on one side and (e) or (m) SMCCs markers on an adjacent area. eSMCC and Mix-associated phenotypes were characterized by a low proliferative index (<15% in the metastatic area) and significant phosphorylation of the histone variant H2AX compared to mSMCC and negative groups (Figure 5d,e).

Kaplan–Meier curves showed that eSMCC-Mix patients had improved overall survival versus the non-expressing group (Figure 5f), indicating this phenotype's beneficial role in limiting cancer progression. Notably, the eSMCC-Mix signatures also significantly impacted the risk of relapse (Figure 5g). In DFS, negative and mSMCCs groups acted distinctly, suggesting that mSMCC-like markers had the worst survival and a principal role in recurrence. Depending on the heterogeneity of therapeutic tools and the limited number of cases randomized in subgroups, we could not establish an impact of chemotherapy in CRLM samples.

To overcome those limits, we investigated the predictive role of the SMCC signatures on The Cancer Genome Atlas database, over an extended group of 362 colon and rectal adenocarcinoma cases. Based on eSMCC versus mSMCC DEG, we selected the genes with *p*-value adj <0.05. After that, for both e/mSMCC groups, we selected the top one hundred genes according to log2FC. We confirmed a significant association between the $eSMCC^{high}$ signature and improved survival in CRC patients (Figure 5h): indeed, >60% of $eSMCC^{high}$ patients survived more than 150 months; in contrast, only 20% of patients presenting with an $eSMCC^{low}$ signature reached this goal (hazard ratio [HR] = 0.55). Furthermore, the disease-free survival curve indicated that $eSMCC^{high}$ patients had less than a 50% chance of cancer recurrence (Figure 5i; HR = 0.55, $p=0.051$). These findings supported the notion of a beneficial role for the $eSMCC^{high}$ signature in primary and corresponding metastatic tumors, as well as its validity as a prognostic marker.

In contrast, the $mSMCC^{high}$ signature was predictive of a worse prognosis for CRC: overall survival indicated that $mSMCC^{high}$ patients were 40% more likely to die within the first 8 years versus $mSMCC^{low}$ patients (Figure 5j; HR = 1.4, pHR = 0.23). These patients had almost twice the chance of cancer relapse versus $mSMCC^{low}$ patients (Figure 5k; HR = 1.9, pHR = 0.043). These findings underscored the poor prognostic value of the mSMCC signature. Of note, there was no correlation between the eSMCC signature and the type of chemotherapy (Figure 5l). Instead, for the mSMCC signature, there was a significant correlation with pharmacological treatment: oxaliplatin and fluorouracil were determinants in the establishment of the highest mSMCC expression (Figure 5m).

Finally, we identified SMCCs in a demonstrative ST analysis of human CRC available at 10× Genomic's website. This analysis demonstrated the reproducibility of our approach over independent experiments, confirming the existence of SMCC populations in primary CRC. At least another tumoral cluster (indicated as not-SMCCs) was identified without any significant prognostic value (Figure S5a,c), as for iSMCCs signature over TCGA database (data not shown).

2.6 | Opposing carcinoma immune ecosystems develop from epithelial and mesenchymal *SMCCs*

We then determined the cellular composition of the local microenvironment. EcoTyper—a machine-learning framework for large-scale identification of cell states and multicellular communities (Luca et al., 2021)—assigned specific carcinoma ecosystems (CEs) within meta1. CEs have predictive cellular, genomic, and clinical outcomes that are strongly conserved across 16 types of human carcinomas. This approach extrapolated three clinically distinct CEs localized in specific metastatic areas: CE1 was characterized by stimulation of CAF transcription, a high risk of death, M2-like macrophages, and lymphocyte deficiency, and was mainly identified in mesenchymal ECM (Figure 6a); in contrast, CE9 and C10 were characterized by strong immunoreactivity, associated with longer overall survival, were typical of highly infiltrated tumors, and represented at the perimetastatic boundaries (Figure S6a,b). To confirm the CE1 phenotype and to overcome the technical gap in the single-cell resolution of ST, we clustered our spatial data with two single-cell databases (Figure S6c–f, workflow). The integration between ST data and single-cell atlas of primary CRCs and liver metastasis (Che et al., 2021) revealed an overlap between the CAF signature and mesenchymal ECM, a phenotype absent in the epithelial area (Figure 6b). We then integrated our spatial stromal transcriptome with single-cell RNA-seq data of treated CRLM-derived immune subpopulations (Che et al., 2021). As expected, M2-phenotype macrophages were present in correspondence with the CE1 ecosystem (Figure 6c and Figure S6g,h). Colony-stimulating factor 1 (*CSF1*) and C-X-C motif chemokine ligand 1 (*CXCL1*), known to attract macrophages and neutrophils, were significantly upregulated in mesenchymal crypts (Figure S6i,j), as well as several immunosuppression-related genes (Cagnoni et al., 2021; Chiavarina et al., 2021; Liu et al., 2018; Patry et al., 2015) (Figure 5e–g). CAFs and M2 macrophages are known to produce TGFβ (Tauriello et al., 2022). Therefore, we reasoned that since in our setting those populations were spatially identified in mSMCC surrounding and physically overlapped (Figure S6l,m), they would be the primary source of TGFβ and mSMCC induction.